Modal Analysis of Acoustic Directivity in Turbulent Jets

Akhil Nekkanti* and Oliver T. Schmidt†
University of California San Diego, La Jolla, California 92093

The directivity of noise from three large-eddy simulations of turbulent jets at Mach 0.7, 0.9, and 1.5 is investigated using spectral proper orthogonal decomposition (SPOD). The most energetic patterns of acoustic radiation are extracted using the far-field pressure 2-norm. Specialization of the norm to the far field is accomplished through localized spatial weighting. Radiation patterns to specific jet inlet angles are isolated by further restricting the spatial weighting to small rectangular regions in the far field. The most energetic radiation pattern for all cases and relevant frequencies is a single superdirective acoustic beam in the downstream direction. The source region of these beams is traced back to the end of the potential core for low frequencies and the shear-layer region for higher frequencies. In the sideline direction, to low angles, the acoustic patterns consist of beams that propagate upstream or perpendicular to the jet axis. The sideline radiation patterns are found to originate from the same source locations as the dominant superdirective beams. Inspection of the SPOD modes reveals that sideline radiation is directly linked to directive downstream radiation. Within the restricted radial extent of the computational domain, these results indicate that the sources of sideline and downstream radiation are intimately linked.

Nomenclature

c	=	speed of sound
D	=	nozzle diameter
f	=	frequency
M_j	=	jet Mach number
m	=	azimuthal wavenumber
n_{blk}	=	number of blocks (or independent realizations)
n_{freq}	=	number of Fourier realizations
n_t	=	number of snapshots
p	=	pressure
Re	=	Reynolds number
St	=	jet Strouhal number, fD/U_j
$St_{\max}$	=	maximum Strouhal number of the postprocessing
T	=	temperature
t	=	time
U	=	axial velocity
W	=	weight matrix
x_c	=	length of the potential core
$\lambda_{f_k}^{(j)}$	=	eigenvalue of the jth mode at kth frequency
μ	=	dynamic viscosity
ρ	=	density
ϕ	=	jet inlet angle, i.e., angle with respect to the upstream jet axis (negative x axis)
$\psi_{f_k}^{(j)}$	=	jth spectral proper orthogonal decomposition mode at kth frequency
Ω	=	computational domain, $x, r \in [0, 30] \times [0, 6]$

Subscripts

j	=	nozzle exit
∞	=	ambience

I. Introduction

THE reduction of jet noise is an important objective for the aviation community. The pioneering works by Crow and Champagne [1] and Brown and Roshko [2] were the earliest to report the presence of large-scale coherent structures in turbulent jets and shear layers, respectively. Here, "large-scale" refers to dimensions longer than or comparable to the jet diameter. Mollo-Christensen [3] described them as intermittent spatial structures, or wavepackets, present in the mixing layer. Researchers [4–8] have modeled the coherent structures as growing and decaying instability waves of the turbulent mean flow. These wavepackets were identified as the main source of aft-angle noise [9]. The acoustic radiation of wavepackets is highly directive and concentrated in the downstream direction. The directive emission shows an exponential decay at high polar angles θ, or low jet inlet angles $\phi = 2\pi - \theta$, correspondingly. This pattern was termed "superdirective radiation" by Crighton and Huerre [8]. In this work, we will use this word more loosely and refer to radiation patterns that are isolated and clearly directed downstream as superdirective. Cavalieri et al. [10] have shown that the axisymmetric mode of the subsonic jets exhibits superdirectivity. Readers can refer to the work of Jordan and Colonius [9] for a comprehensive review on wavepackets in turbulent jets.

Based on experimental observations and the authors' physical interpretation of the source mechanisms, Tam et al. [11] proposed a separation of the far-field spectrum into two empirical similarity spectra for the downstream and sideline radiation, respectively. This approach was later extended to subsonic jets by Viswanathan [12,13] and Tam et al. [14].

Wavepackets and their role in the generation of jet noise have been studied extensively using various methods of linear stability analysis and other perturbation formulations. Global stability analyses [15,16], solutions to the parabolized stability equations [17–20], and the one-way Navier–Stokes equations [21] have consistently identified Kelvin–Helmholtz (KH) instability waves and associated them with downstream radiation patterns. Numerical evidence for upstream traveling acoustic wave patterns in global modes has been presented by Nichols and Lele [15] and Schmidt et al. [22]. Similarly, multidirective radiation patterns that include sideline and upstream radiation have been identified using resolvent analysis [23–26]. The validity of classical linear stability theory and resolvent analysis applied to mean flows has been confirmed by comparison with empirical modes obtained from high-fidelity simulation data using spectral proper orthogonal decomposition (SPOD) [27,28] and conditional space–time proper orthogonal decomposition [29]. According to the two-source modeling paradigm [14], jet noise in the sideline direction is associated with scales of dimensions much smaller than the jet diameter, referred to as small-scale turbulence by the authors. In accordance with the observation of upstream radiation patterns in modal solutions, as described above, Papamoschou [30] showed that stochastic wavepacket models predict far-field noise at both low and high angles. Hence, even in subsonic and

*Ph.D. Student, Department of Mechanical and Aerospace Engineering. Student Member AIAA.

†Assistant Professor, Department of Mechanical and Aerospace Engineering. Member AIAA.

ideally expanded jets where mechanisms leading to upstream propagation of energy may be absent [31], these results underpin the notion that large-scale coherent structures significantly contribute to sideline and upstream radiation. We provide further empirical evidence for this hypothesis by applying SPOD to educe directional noise.

Modal decomposition techniques [32,33] facilitate the analysis of complex flows by extracting essential features. The most widely used approach, proper orthogonal decomposition (POD), was introduced by Lumley [34,35] to educe coherent structures from turbulent flowfields. Space-only POD computed using the method of snapshots was later introduced by Sirovich [36] and is the most commonly used form of POD. It decomposes the flowfield into temporal coefficients and spatial modes that optimally represent the data in terms of energy. The temporal POD expansion coefficients contain, in general, a combination of different time scales and are only correlated at zero time lag. SPOD is the frequency-domain variant of POD. It computes modes that oscillate at a single frequency from statistically stationary data. By construction, SPOD identifies structures that are coherent in both space and time [27] (in the strict mathematical sense). A number of studies showed that the dominant dynamics are often accurately captured by only a few modes [27,28,37–39]. Experimentally, Glauser et al. [37], Citriniti and George [38], and Jung et al. [39] showed that a large fraction of the kinetic energy is contained in the first three SPOD modes. Recently, Schmidt et al. [28] applied SPOD to high-fidelity simulation data of turbulent jets in the subsonic, transonic, and supersonic regimes. The authors give a detailed account of the KH and the Orr-type instability mechanisms that dominate the initial shear layer and the region downstream of the potential core, respectively. Towne et al. [27] performed SPOD on Mach 0.4 turbulent jet and present a detailed account of the method and its relationship to space-only POD, resolvent analysis, and dynamic mode decomposition (DMD).

In the present study, we perform SPOD of large-eddy simulation (LES) simulation data of jets at Mach 0.7, 0.9, and 1.5, and analyze radiation wave patterns with special emphasis on directivity. The remainder of this paper is arranged as follows. In Sec. II, the methodology is recapitulated. In Sec. III, the results are presented and the work is summarized in Sec. IV.

II. Spectral Proper Orthogonal Decomposition

SPOD computes monochromatic modes that are optimally ranked by energy. Because of the optimality and coherence properties, SPOD modes often represent the dynamically most relevant and prevailing flow structures. Given a flowfield $\boldsymbol{q}_i = \boldsymbol{q}(t_i) \in \mathbb{C}^n$, where $\boldsymbol{q}$ represents a wide-sense stationary process that is sampled at n_t discrete time instances $t_1, t_2, \ldots, t_{n_t}$, the data matrix $\boldsymbol{Q}$ of the fluctuating field is defined as

$$\boldsymbol{Q} = \left[\boldsymbol{q}_1 - \bar{\boldsymbol{q}}, \boldsymbol{q}_2 - \bar{\boldsymbol{q}}, \ldots, \boldsymbol{q}_{n_t} - \bar{\boldsymbol{q}}\right] \in \mathbb{C}^{n\times n_t} \tag{1}$$

Here, $\bar{\boldsymbol{q}}$ denotes the temporal mean. The instantaneous energy $\|\boldsymbol{q}\|_x^2 = \langle \boldsymbol{q}, \boldsymbol{q}\rangle_x$ of a given quantity may be expressed in terms of a spatial inner product

$$\langle \boldsymbol{q}, \boldsymbol{q}\rangle_x = \boldsymbol{q}^* \boldsymbol{W} \boldsymbol{q} = \int_\Omega \boldsymbol{q}^*(x', t)\boldsymbol{q}(x', t)\,\mathrm{d}x' \tag{2}$$

where $\boldsymbol{W}$ is a weight matrix that accounts for numerical quadrature and componentwise weights. $(.)^*$ denotes the complex conjugate. Analogously, the total energy of the quantity is defined via the corresponding space–time inner product

$$\langle \boldsymbol{q}, \boldsymbol{q}\rangle_{x,t} = \int_{-\infty}^{\infty}\int_\Omega \boldsymbol{q}^*(x', t)\boldsymbol{q}(x', t)\,\mathrm{d}x' t \tag{3}$$

To estimate the cross-spectral density, we use Welch's [40] approach and segment the data into n_{blk} overlapping blocks. The lth block,

$$\boldsymbol{Q}^{(l)} = [\boldsymbol{q}_1^{(l)} - \bar{\boldsymbol{q}}, \boldsymbol{q}_2^{(l)} - \bar{\boldsymbol{q}}, \cdots, \boldsymbol{q}_{n_{\text{freq}}}^{(l)} - \bar{\boldsymbol{q}}] \in \mathbb{C}^{n\times n_{\text{freq}}} \tag{4}$$

contains n_{freq} snapshots as its columns. Each block is considered a statistically independent realization under the ergodic hypothesis. Next, the row-wise discrete Fourier transform is performed on each block to yield

$$\hat{\boldsymbol{Q}}^{(l)} = [\hat{\boldsymbol{q}}_1^{(l)}, \hat{\boldsymbol{q}}_2^{(l)}, \ldots, \hat{\boldsymbol{q}}_{n_{\text{freq}}}^{(l)}] \in \mathbb{C}^{n\times n_{\text{freq}}} \tag{5}$$

By $\hat{\boldsymbol{q}}_i^l$ we denote the lth Fourier realization at ith discrete frequency. We proceed by arranging all Fourier realizations at a fixed frequency f_k in a matrix

$$\hat{\boldsymbol{Q}}_{f_k} = [\hat{\boldsymbol{q}}_{f_k}^{(1)}, \hat{\boldsymbol{q}}_{f_k}^{(2)}, \ldots, \hat{\boldsymbol{q}}_{f_k}^{(n_{blk})}] \in \mathbb{C}^{n\times n_{\text{blk}}} \tag{6}$$

The cross-spectral density matrix at each frequency is then calculated as

$$\boldsymbol{S}_{f_k} = \hat{\boldsymbol{Q}}_{f_k}\hat{\boldsymbol{Q}}_{f_k}^* \in \mathbb{C}^{n\times n} \tag{7}$$

The eigenvalue decomposition of the cross-spectral density matrix

$$\boldsymbol{S}_k W \boldsymbol{\psi}_{f_k} = \boldsymbol{\psi}_{f_k}\boldsymbol{\Lambda}_{fk} \tag{8}$$

yields the SPOD modes, $\boldsymbol{\Psi}(x)$. The mode energies are the corresponding eigenvalues on the diagonal of $\boldsymbol{\Lambda}_{f_k} = \mathrm{diag}(\lambda_{f_k}^{(1)}, \lambda_{f_k}^{(2)}, \ldots \lambda_{f_k}^{(n)})$, where $\lambda_{f_k}^{(1)} \geq \lambda_{f_k}^{(2)} \geq \ldots \geq \lambda_{f_k}^{(n)}$. The first SPOD mode contains the largest fraction of the total energy at each frequency and is often referred as the leading or optimal mode. Subsequent modes are referred to as suboptimal modes. The SPOD modes are orthogonal at the same frequency, i.e.,

$$\boldsymbol{\psi}_{f_k}^* W \boldsymbol{\psi}_{f_k} = I \in \mathbb{R}^{n_{\text{blk}}\times n_{\text{blk}}} \tag{9}$$

where $\boldsymbol{I}$ is the identity matrix. The ability of SPOD to decouple the dynamics from different time scales makes the results highly interpretable.

III. Results and Discussion

We analyze the LES databases of turbulent jets at Mach numbers $M_j = 0.7$, 0.9, and 1.5 computed by Brès et al. in [41–43], respectively. The reader is referred to Brès et al. [41–43] for further details on the numerical method and meshing strategy. The flow is nondimensionalized by the nozzle exit values, namely, velocity by U_j, pressure by $\rho_j U_j^2$, length by the nozzle diameter D, and time by D/U_j. Frequencies are reported in terms of the Strouhal number $St = fD/U_j$. A cylindrical domain Ω of size $x, r \in [0, 30]\times[0, 6]$ is used for the analysis. The LES data consist of 10,000 snapshots separated by a time step of $\Delta t c_\infty/D$. Important parameters are summarized in Table 1.

Previous studies [9,10,44–46] have reported that most of the far-field sound energy is concentrated in the first three azimuthal wavenumbers, $m = 0, 1$, and 2. For the sound radiated in the downstream direction, the axisymmetric mode ($m = 0$) is most dominant, whereas the helical ($m = 1$) and the double-helical modes ($m = 2$) become more important in the sideline direction [9]. In this study, we focus our attention on the noise emitted by these three azimuthal wavenumbers. The directivity of the radiation is expressed in terms of the jet inlet angle ϕ, defined with respect to the negative x axis, such that 180° corresponds to the downstream direction and 90° to the sideline direction perpendicular to the jet axis.

The intensity of the sound radiated to different directions is computed by calculating the overall sound pressure level (OASPL) along the upper boundary at $r = 6$. At this radial distance, effects of the hydrodynamic pressure component are still partially present, in particular for low frequencies and downstream of the potential core (see also [47,48]). Acoustic analogies based on Kirchhoff's method [49] or the Ffowcs Williams–Hawkings equations [43,50] may in principle be applied to extend the analysis to the true far field, but this is beyond the scope of this study. Here, the noise at the radial distance

Table 1 Parameters of the large-eddy simulations

Case	Re	M_j	T_j/T_∞	p_0/p_∞	$\Delta t c_\infty/D$	$St_{\max}$	Reference
Supersonic	1.55×10^5	1.5	1.74	3.67	0.1	1.0	Case A2 [43]
Transonic	1.01×10^6	0.9	1.0	1.7	0.2	1.6	[42]
Subsonic	0.79×10^6	0.7	1.0	1.4	0.2	1.6	[41]

$r = 6$ is used as a proxy of the far-field pressure. The power spectral density and the OASPL are defined as

$$\mathrm{PSD} = 10\log_{10}\left(\frac{2\hat{p}'(m,\phi,St)\hat{p}'^{*}(m,\phi,St)}{p_{\mathrm{ref}}^2 St_{\min}}\right), \quad \text{and} \tag{10}$$

$$\mathrm{OASPL} = 10\log_{10}\left(\sum_{St_{\min}}^{St_{\max}}\frac{2\hat{p}'(m,\phi,St)\hat{p}'^{*}(m,\phi,St)}{p_{\mathrm{ref}}^2}\right) \tag{11}$$

respectively. Here, p_{ref} is the reference pressure and $\hat{p}'$ is the Fourier transform of the pressure fluctuations in time.

The PSD is estimated using the Welch's method [40] with 50% overlap and $n_{\mathrm{freq}} = 512$. Within the radial extent of the computational domain ($r \le 6$) and at high jet inlet angles, the hydrodynamic component contributes a significant part of the energy associated with pressure fluctuations [51]. To eliminate the effect of the hydrodynamic component, a high-pass filter ($St \ge 0.1$) is used. The OASPLs of the filtered signals for different azimuthal wavenumbers and different Mach numbers are presented in Fig. 1. The OASPL at each ϕ is a measure of the total sound radiated in that particular direction. The OASPL of azimuthal mode $m = 1$ peaks at $\phi = 156°$ for the supersonic jet, whereas the $m = 0$ component peaks at $\phi = 162°$ for the transonic and subsonic jets. These angles are in agreement with the observations made by Jordan and Colonius [9] and Tam et al. [14]. For the supersonic jet, the $m = 1$ component dominates at most angles. At lower inlet angles, $m = 2$ is the leading subdominant component. At higher angles, this component is replaced by $m = 0$. In the case of the transonic jet, $m = 1$ is the most dominant component in the range $90° \le \phi \le 155°$, whereas $m = 0$ is the most dominant component for $\phi \ge 155°$. For subsonic jets, the OASPL curves in Fig. 1c show that $m = 0$ is clearly the most dominant mode, followed by $m = 1$ and then $m = 2$. For all the three jets, the $m = 1$ component is larger than the $m = 2$ contribution. With increasing azimuthal wavenumber, the peak OASPL shifts toward lower jet inlet angles.

The scatter plot in Fig. 2 shows the variation of the maximum PSD as a function of the jet inlet angle. False colors show the corresponding Strouhal number. Similar trends as for the OASPL are observed; see Fig. 1. The false color indicates the frequency with the largest contribution to the PSD at each angle. It can be seen that the frequency of the peak PSD is $St = 0.4$ for the supersonic case and $St = 0.2$ for the transonic and subsonic cases, respectively. In particular for the supersonic jet, it is observed that lobes in the PSD at high jet angle correspond to distinct frequency bands. In all three cases, the axisymmetric azimuthal component peaks at $\phi \approx 160°$ and $St \approx 0.2$. The presence of discrete color bands in Fig. 2 suggests a clear relationship between radiation angle and frequency.

The SPOD eigenvalues and modes are computed for the pressure. The pressure 2-norm is used as a proxy of the acoustic energy in the far field. To isolate contributions to the far field, we choose a weighting function

$$W(x) = \begin{cases} 1 & \text{for } 5 \le r \le 6,\ \forall\ x \in \Omega \\ 0 & \text{otherwise} \end{cases} \tag{12}$$

Figure 3 shows the SPOD spectra for all cases and azimuthal wavenumbers under consideration. Below $St = 0.1$, the far-field pressure partially consists of hydrodynamic fluctuations. As we are interested in acoustics, we omit this region for clarity. Parts of some of the spectra exhibit a large difference between the first (optimal or leading) and second (first suboptimal) modes. This behavior is referred to as low-rank behavior [28] and indicates dominance of a physical mechanism associated with the first mode. It is most pronounced for the axisymmetric component within the ranges $0.1 \le St \le 0.6$ and $0.1 \le St \le 0.7$ for the transonic and subsonic jets, respectively. The prevalence of this behavior decreases as m increases. The frequency at which the low-rank behavior peaks is termed as the "dominant frequency." Modes at representative frequencies and azimuthal wavenumbers are shown in Fig. 4. In particular, we pick the maximum OASPL azimuthal wavenumber; see Fig. 1. The SPOD modes clearly indicate the dominance of superdirective acoustic radiation emanating from the end of the potential core as the main source location of high inlet-angle jet noise. It is important to note that the patterns of the SPOD modes imply spatial correlation, but not causation. Because of the acoustic nature of the problem, the SPOD modes clearly reveal the source location, but not necessarily the source mechanism. In the particular case of turbulent jets, however, the primary source of the superdirective radiation has previously been identified as the KH-type annular instability of the jet shear-layer, using stability-theoretical tools [15,21,28]. The pressure signature of a KH wavepacket is clearly visible in the supersonic jet for $m = 1$ (top panel of Fig. 4a).

The radiation patterns confirm the relationship between the jet inlet angle and frequency previously discussed in the context of Fig. 2. Directive beams that propagate at steeper angles are observable at the higher frequencies of $St = 0.6$ and $St = 1.0$ (middle and bottom rows of Fig. 4). The first, second, and third suboptimal modes at $St = 0.6$ are shown in Fig. 5. Multiple directive beams are observed for all the jets. The number of beams increases with mode number. The suboptimal mode of the transonic and subsonic jets exhibits two superdirective beams. These beams originate from

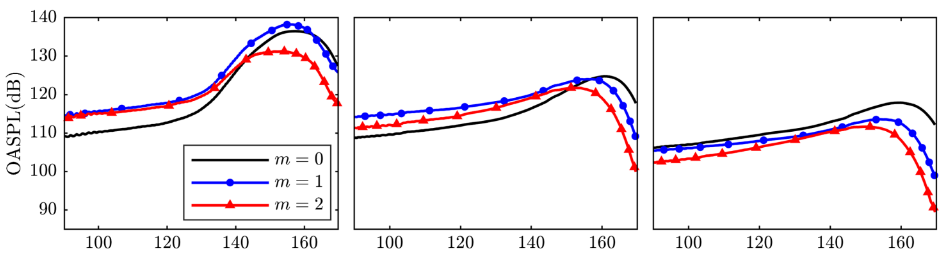

a) Supersonic jet $M_j = 1.5$ **b) Transonic jet $M_j = 0.9$** **c) Subsonic jet $M_j = 0.7$**

Fig. 1 Overall sound pressure level at different jet inlet angles. OASPL for $m = 0$ (black solid lines), $m = 1$ (blue lines with circles). and $m = 2$ (red lines with triangles).

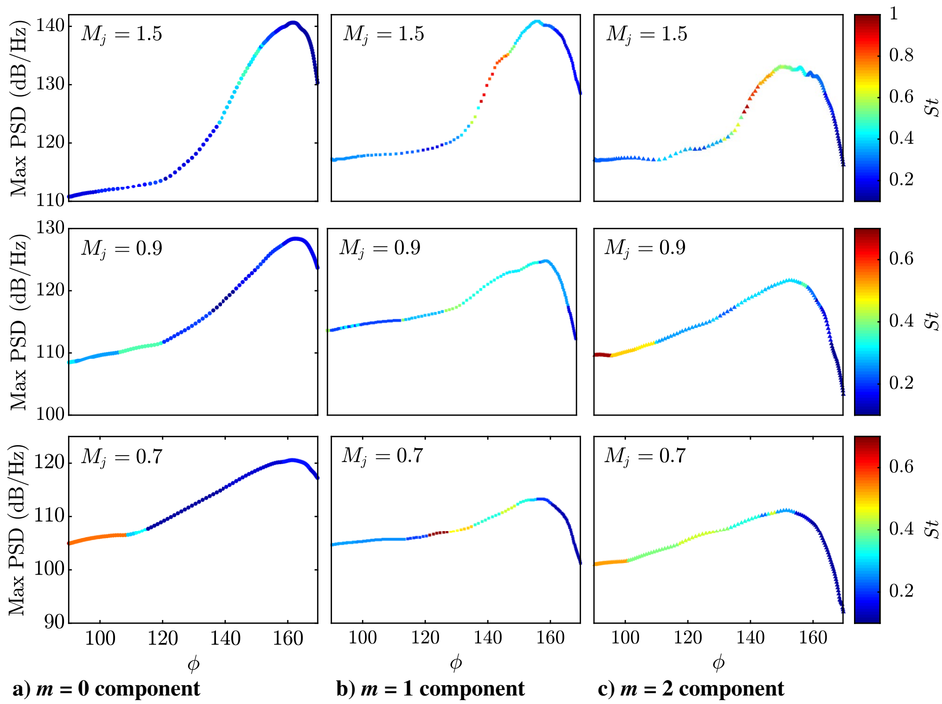

Fig. 2 Maximum PSD as a function of jet inlet angle: $m = 0$, $m = 1$, and $m = 2$. False colors indicate corresponding peak frequency. The relative trends between different azimuthal components are identical to Fig. 1.

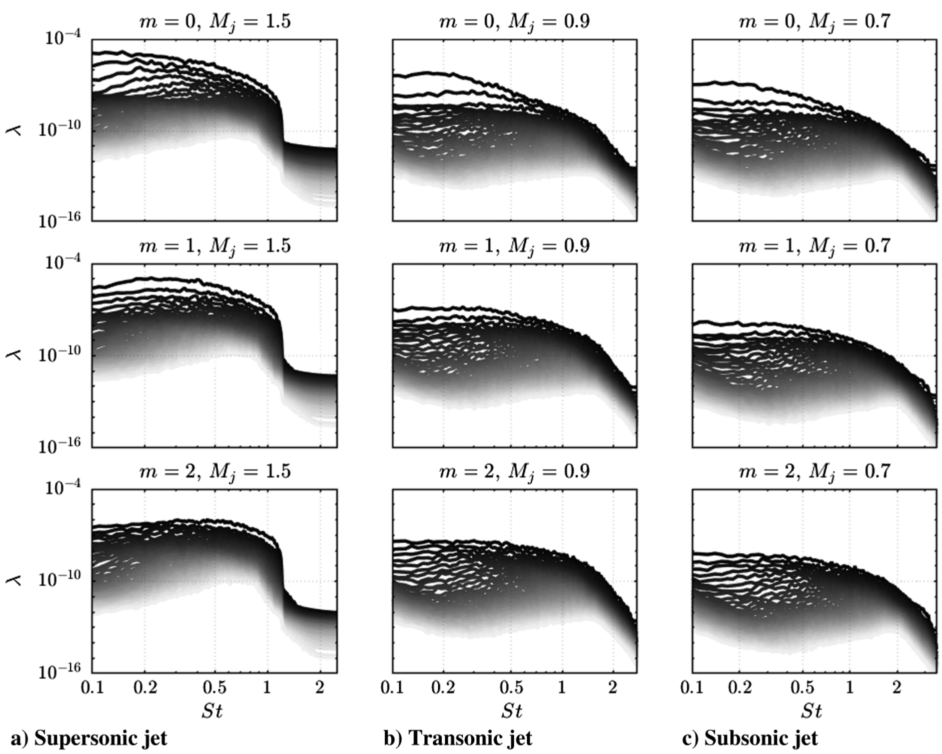

Fig. 3 SPOD eigenvalue spectra for the far-field focus region as defined in Eq. (12).

either side of the end of the potential core. Rigas et al. [21] suggest that these two beams originate from the KH wavepacket and the Orr-type waves, respectively [28,52]. The higher suboptimal modes of the transonic and subsonic jets (middle and bottom rows of Figs. 5b and 5c) exhibit upstream and sideline propagating radiation. In Sec. III.B, this observation is addressed in more detail. Notably, very similar radiation patterns have been predicted by Jeun et al. [23] using resolvent analysis and global modes by Schmidt et al. [16].

The distinct radiation patterns identified by the leading SPOD modes may be leveraged to locate their origin. We obtain an estimate of this location by finding the absolute maximum of the pressure modes along the lipline, $r = 0.5$. This corresponds to the radial distance of maximum turbulent activity close to the nozzle, but we note that the beam tracing does not depend on the exact radial location. Figure 6 shows the beam origin as a function of the Strouhal number for the transonic jet and different azimuthal wavenumbers. We focus on the transonic case for comparison with literature. In agreement with the findings of [47,48,53], high-frequency radiation patterns originate near the nozzle exit, whereas the low-frequency acoustic beams emanate from a location further

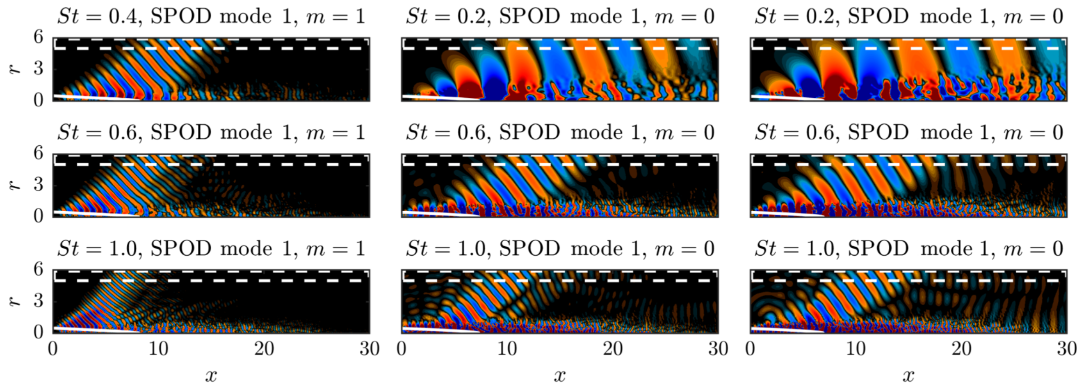

a) Supersonic jet $M_j = 1.5$ b) Transonic jet $M_j = 0.9$ c) Subsonic jet $M_j = 0.7$

Fig. 4 Leading SPOD modes at peak frequencies (top row), for $St = 0.6$ (middle row), and for $St = 1.0$ (bottom row). The focus region is indicated by the dashed white box. White solid lines represent the edge of the potential core defined as $\bar{u}(x,r) = 0.95U_j$, where $\bar{u}$ is the mean axial velocity.

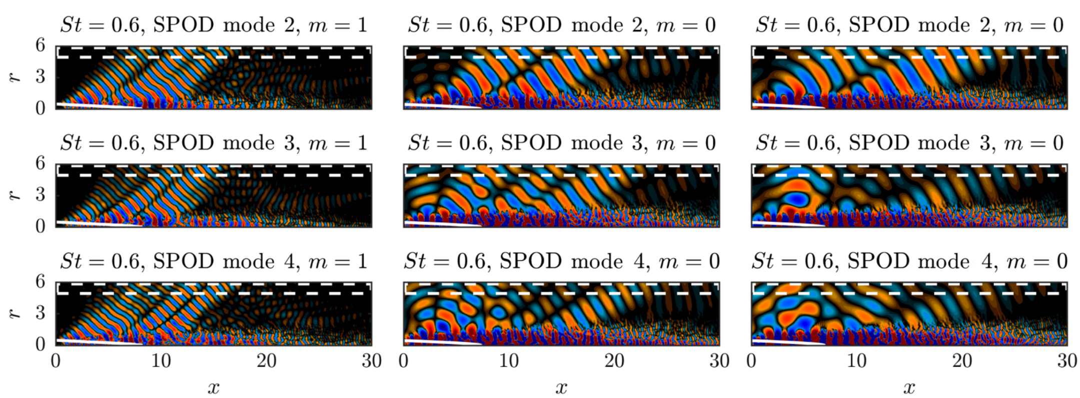

a) Supersonic jet $M_j = 1.5$ b) Transonic jet $M_j = 0.9$ c) Subsonic jet $M_j = 0.7$

Fig. 5 First, second, and third suboptimal SPOD modes at $St = 0.60$. The focus region is indicated by the dashed white box. White solid lines represent the edge of the potential core defined as $\bar{u}(x,r) = 0.95U_j$, where $\bar{u}$ is the mean axial velocity.

downstream. Previous studies on acoustic source localization [47,54,55] and wavepacket modeling [28,56] have shown that the frequency scales with $St \sim 1/x$ in the shear layer region. A least-square fit for this scaling is shown for the first three azimuthal wavenumbers. In the bottom row of Fig. 6, this curve fit is compared with the approximate source locations found experimentally by Bogey et al. [48] for a comparable jet using the method of Zoppellari et al. [57]. Note that the full pressure signal used in the work of Bogey et al. [48] is compared with different azimuthal components. A good match between the literature and the present results is observed.

Next, we examine the dominant radiation patterns for different angles by introducing a new weighting function $W_f(x)$ that focuses on small boxes that are representative of specific angles:

$$W_f(x) = \begin{cases} 1 & \text{for } 5 \leq r \leq 6, x_f - 0.5 < x < x_f + 0.5, \text{where } x_f \in [0.5, 29.5], \\ 0 & \text{otherwise} \end{cases} \tag{13}$$

The center of each box of height and width $\Delta x = 1.0$ is used to calculate the angle. The PSD and SPOD spectrum for different jet inlet angles are compared in Fig. 7. This comparison is shown for $m = 0$. Similar trends are observed for higher azimuthal wavenumbers as well. To facilitate direct comparison with PSD, the SPOD spectrum is normalized by the area of the box. The leading SPOD mode (blue dotted line) is able to predict the PSD (black lines) accurately, in particular at low frequencies. The total SPOD energy is obtained as the sum of all SPOD eigenvalues and shown as red lines. Only a marginal improvement of the comparison over the leading mode energy is observed. The energy contained in the leading SPOD mode is found to account for at least 90% of the total energy over all frequencies. This shows that the radiation to specific angles is dominated by a specific source. Another conclusion is that a rank-1 SPOD approximation yields an accurate model of the directional radiation.

Figure 8b shows the area-weighted eigenvalue of the leading SPOD mode as a function of frequency and inlet angle. The spectrum closely resembles the PSD of the raw pressure data shown in Fig. 8a. For brevity, only the $m = 0$ component of the supersonic jet is shown, but similar results are found for all other cases. The OASPL calculated from the data and the area-weighted SPOD energy of the first mode are compared in Figs. 9a–9c. The OASPL is calculated as in Eq. (9) using the spectrum shown in Fig. 8b. The rank-1 SPOD approximation follows the trend of the OASPL well. Jeun and Nichols [26] made similar observations for a rank-1 approximation based on resolvent analysis. For the two lower-Mach-number jets, the OASPL curves predicted by the rank-1 approximation are more accurate than in the supersonic case.

A. Superdirective Radiation

SPOD eigenvalue spectra for a focus region corresponding to the location of the peak OASPL (see Table 2) are shown in Fig. 10. All of these spectra exhibit a low-rank behavior in the frequency range $0.1 \leq St \leq 1.0$. The optimal and the suboptimal eigenvalues differ

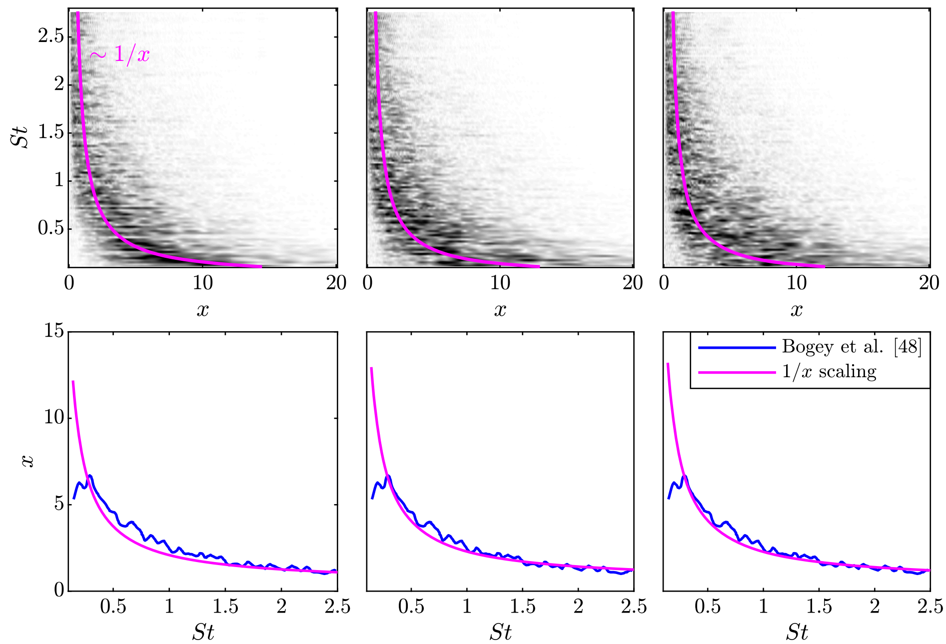

a) m = 0 component b) m = 1 component c) m = 2 component

Fig. 6 The source locations of the acoustic beams for the transonic jet $M_j = 0.9$ and azimuthal wavenumber a) $m = 0$, b) $m = 1$, and c) $m = 2$. Top row denotes the normalized intensity of the SPOD modes (, black, gray, white, $0 \leq \psi/\|\psi\|_\infty \leq 1$) along the lipline $r = 0.5$. Least square fit of the scaling $St \sim 1/x$ is denoted by magenta lines. The location of the maximum intensity as a function of the St is shown in the bottom row. The scaling is compared with the experimental results by Bogey et al. [48].

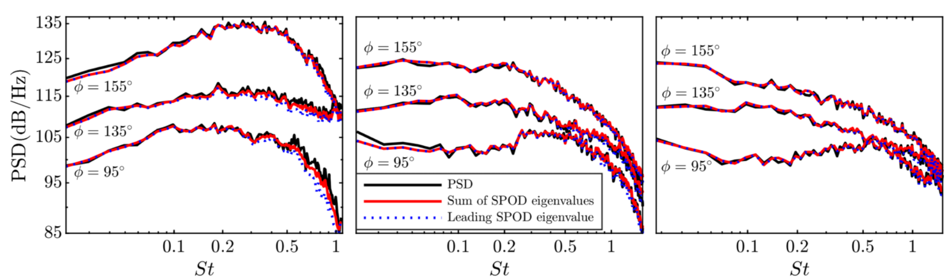

a) Supersonic jet $M_j = 1.5$ b) Transonic jet $M_j = 0.9$ c) Subsonic jet $M_j = 0.7$

Fig. 7 Comparison of PSD and SPOD spectra for the $m = 0$ component. Black lines represent the PSD, blue dotted lines represent the first SPOD mode, and red lines represent the sum of all SPOD modes.

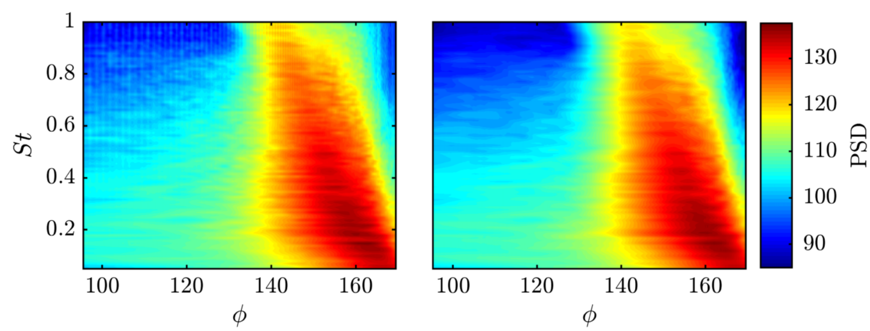

a) Time series b) Rank-1 approximation

Fig 8 PSD estimated from the a) time series of the LES pressure data and b) leading SPOD eigenvalue for $m = 0$ of the supersonic jet.

by up to three orders of magnitude in this band. This observation indicates that most of the energy is present in the first mode and is consistent with the results shown in Fig. 7. The leading SPOD modes at the peak frequencies are shown in the top row of Fig. 11. It is observed that the peak frequencies from the SPOD analysis and the peak PSD frequency coincide. This implies that the leading SPOD mode provides an accurate representation of the directive far-field radiation. Superdirective beams that encompass the region being investigated are observed. For the lower-Mach-number jets, the acoustic beams originate from the end of the potential core, whereas this location appears to be shifted slightly upstream in the supersonic case. The observations made for $M_j = 0.9$ are in agreement with the findings of Bogey and Bailly [58]. The superdirective radiation propagates at a steeper angle in the supersonic jet. The steeper propagation angle and upstream source location appear to cause a shift in the maximum directivity toward a lower jet inlet angle for the supersonic jet. Cavalieri et al. [10] argue that the azimuthal interference of the helical mode and the smaller spatial extent of the helical

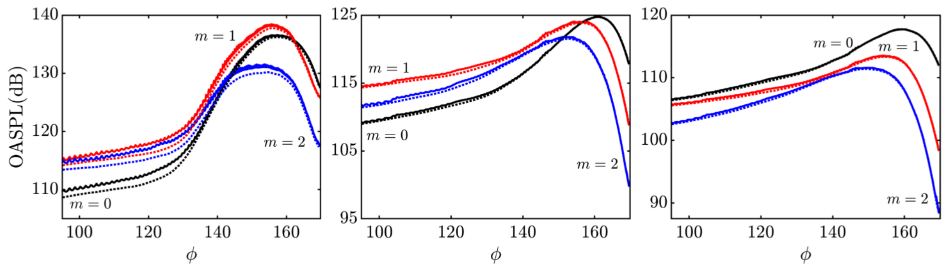

a) Supersonic jet $M_j = 1.5$ b) Transonic jet $M_j = 0.9$ c) Subsonic jet $M_j = 0.7$

Fig. 9 Comparison between OASPL of the LES pressure data (solid lines) and leading SPOD eigenvalue (dotted lines): $m = 0$ (black), $m = 1$ (red), and $m = 2$ (blue).

Table 2 Maximum OASPL and radiation angles for the different cases

	Subsonic $M_j = 0.7$		Transonic $M_j = 0.9$		Supersonic $M_j = 1.5$	
Azimuthal wavenumber	ϕ, °	$\mathrm{OASPL_{max}}$, dB	ϕ, °	$\mathrm{OASPL_{max}}$, dB	ϕ, °	$\mathrm{OASPL_{max}}$, dB
$m = 0$	161.8	117.7	162.0	124.8	158.1	136.6
$m = 1$	154.1	113.5	157.0	124.1	155.7	138.5
$m = 2$	149.4	111.6	151.4	121.8	150.8	131.5

wavepackets cause this difference. The leading SPOD modes at $St = 0.8$ are shown in the bottom row of Fig. 11. Multiple beams emanating from different source locations are observed in the supersonic and the transonic jet. This decrease of directivity with increasing frequency is in agreement with the findings by Cavalieri et al. [10] and may be attributed to the decline of the dominance of the KH mechanism in this regime.

B. Noise Generated in the Sideline Direction

To understand the generation of jet noise in the sideline direction, we focus our attention to the dominant radiation patterns to angles $\phi < 135°$. These angles represent the region above the potential core. As before, we focus on the azimuthal wavenumber of the peak OASPL in that region (see Fig. 1). Figure 12 depicts the leading SPOD modes for $\phi = 95°$. At the peak Strouhal numbers (top row of Fig. 12), upstream traveling radiation patterns are observed. The SPOD modes of the supersonic and transonic jets also reveal the presence of directive downstream radiation. Both the upstream and downstream radiation patterns originate from the same source location at the end of the potential core. The leading modes at $St = 0.8$ (bottom row of Fig. 12) exhibit multidirective radiation patterns that include upstream, sideline, and downstream beams. In the supersonic case, the upstream radiation is clearly slaved to the much more energetic downstream radiation.

The sideline radiation perpendicular to the jet axis is investigated in Fig. 13. The SPOD was computed by translating the focus region along the upper boundary at an interval of $\Delta x = 0.1$. The angles for which perpendicular radiation patterns are observed were selected

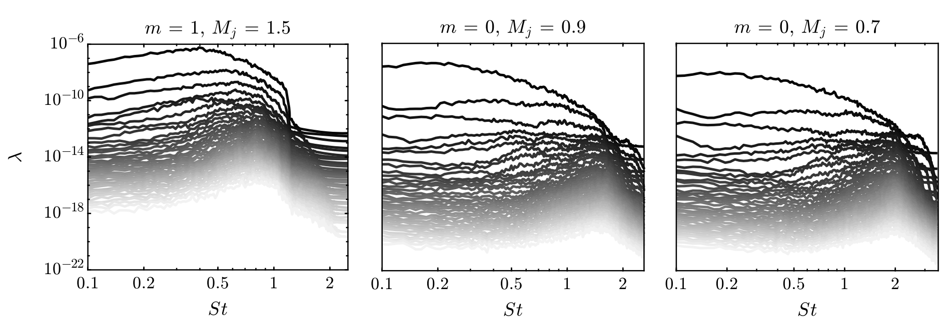

a) Supersonic jet $M_j = 1.5$ b) Transonic jet $M_j = 0.9$ c) Subsonic jet $M_j = 0.7$

Fig. 10 SPOD eigenvalue spectra for the peak OASPL focus region. Spectra are shown for the dominant azimuthal wavenumber of each jet.

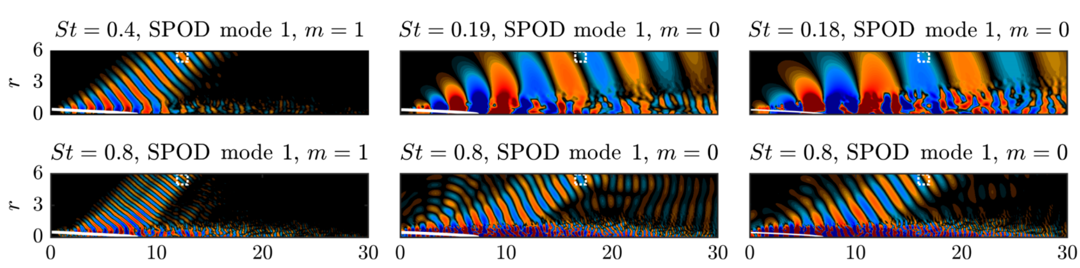

a) Supersonic jet $M_j = 1.5$ b) Transonic jet $M_j = 0.9$ c) Subsonic jet $M_j = 0.7$

Fig. 11 Leading SPOD modes at peak frequencies (top row) and for $St = 0.80$ (bottom row). The focus region is indicated by the dashed white box. White solid lines represent the edge of the potential core defined as $\bar{u}(x,r) = 0.95U_j$, where $\bar{u}$ is the mean axial velocity.

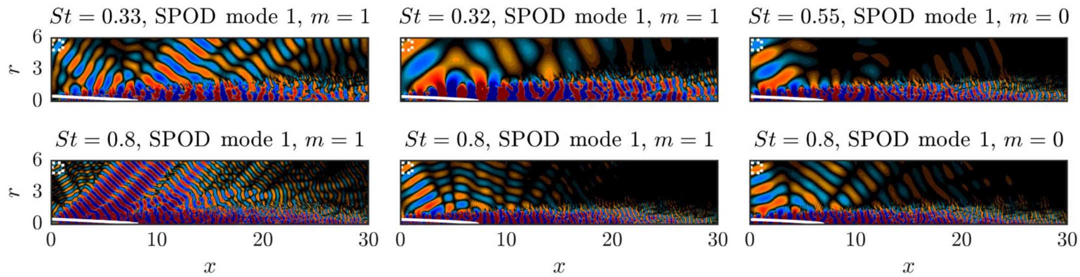

a) Supersonic jet $M_j = 1.5$ **b) Transonic jet $M_j = 0.9$** **c) Subsonic jet $M_j = 0.7$**

Fig. 12 Leading SPOD modes at peak frequencies (top row) and for $St = 0.80$ (bottom row). The focus region is indicated by the dashed white box. White solid lines represent the edge of the potential core defined as $\bar{u}(x,r) = 0.95U_j$, where $\bar{u}$ is the mean axial velocity.

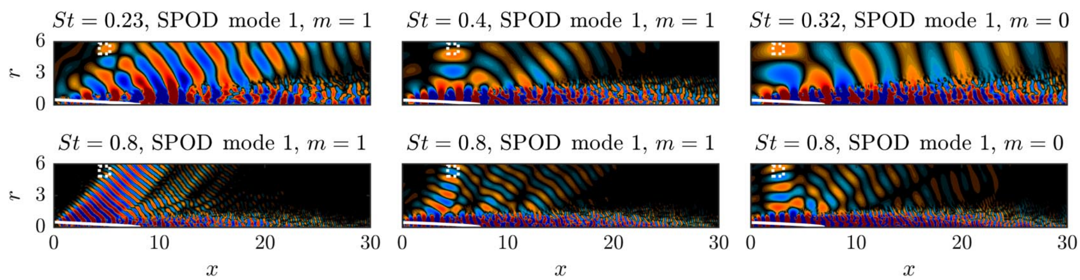

a) Supersonic jet $M_j = 1.5$ **b) Transonic jet $M_j = 0.9$** **c) Transonic jet $M_j = 0.7$**

Fig. 13 Leading SPOD modes at peak frequencies (top row) and for $St = 0.80$ (bottom row). The focus region is indicated by the dashed white box. White solid lines represent the edge of the potential core defined as $\bar{u}(x,r) = 0.95U_j$, where $\bar{u}$ is the mean axial velocity.

manually. Notably, the identified angles of $\phi = 112°$, $\phi = 129°$, and $\phi = 131°$ for the subsonic, transonic, and supersonic jet, respectively, correspond to distinct frequency bands in Fig. 2. All modes also exhibit downstream radiation. For the supersonic jet, the downstream radiation is found considerably more energetic than the sideline beam. Similar to the findings of Freund [59], these observations suggest that the sideline radiation is directly coupled with the dominant directive radiations, implying that both originate from the same source at the end of the potential core. For the higher frequency, $St = 0.8$, the source location is further upstream. This trend can be explained by the fact that the peak location of the KH wavepacket moves upstream with increasing frequency. The leading SPOD modes of the supersonic and the transonic jets at $St = 0.80$ (bottom row of Figs. 13a and 13b) show multidirective radiation patterns.

Next, we inspect the link between downstream and sideline radiation. In Fig. 14, the leading mode at $\phi = 156°$ is compared with a higher mode (lower energy) at $\phi = 95°$ and vice versa. The leading mode corresponding to the region of maximum directivity and the eighth mode at $\phi = 95°$ are observed to resemble each other. Both of these modes exhibit superdirective beams that propagate at the same angle and originate from a similar location in the shear layer. The bottom row of Fig. 14 shows the 10th mode at $\phi = 156°$ and the leading mode at $\phi = 95°$. As before, close correspondence is found. Note that the convergence of these higher SPOD modes is not guaranteed; see Appendix A. However, it was confirmed by manual inspection that the same flow features are consistently found within a narrow range of mode numbers if only a subset of the full data was used. This result clearly suggests that the sideline radiation is directly linked to the dominant downstream radiation pattern. Similar observations are found for the other cases. In summary, the observations made in Figs. 11–14 suggest that downstream and sideline emissions share the same location of origin. An important implication from a modeling perspective is that structures that are found to be dominant for a particular spatial weighting are recovered as suboptimal modes in the other. This means that, if a sufficient number of SPOD modes are retained, the two SPOD bases span a similar space.

Based on a comprehensive analysis of experimental data, Tam et al. [14] suggest the use of two universal curves. The F spectrum, which exhibits a distinct peak at lower frequencies, models radiation to downstream angles. Noise spectra of sideline radiation are generally more broadband and approximated by the so-called G spectrum. The PSDs for two angles representative of sideline radiation (at $\phi = 95°$) and downstream radiation (at $\phi = 160°$) are compared with the G and F spectra, respectively, in Fig. 15. The pressure PSDs of the first three azimuthal wavenumbers contain most of the acoustic energy [9] and are summed here. The PSD curves follow the similarity spectra for all the cases, with small deviations at higher frequencies. The peak frequency of the F spectrum is around

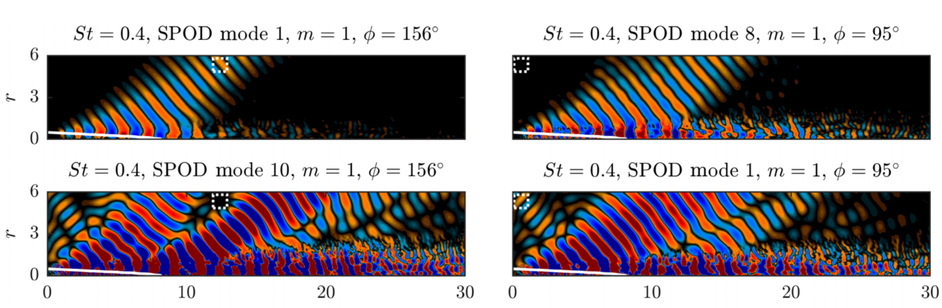

Fig. 14 Comparison of leading and suboptimal SPOD modes for the supersonic jet $M_j = 1.5$ at $St = 0.40$: mode 1 (top left) and mode 10 (bottom left) for $\phi = 156°$; mode 8 (top right) and mode 1 (bottom right) for $\phi = 95°$. The most similar modes were identified by visual inspection.

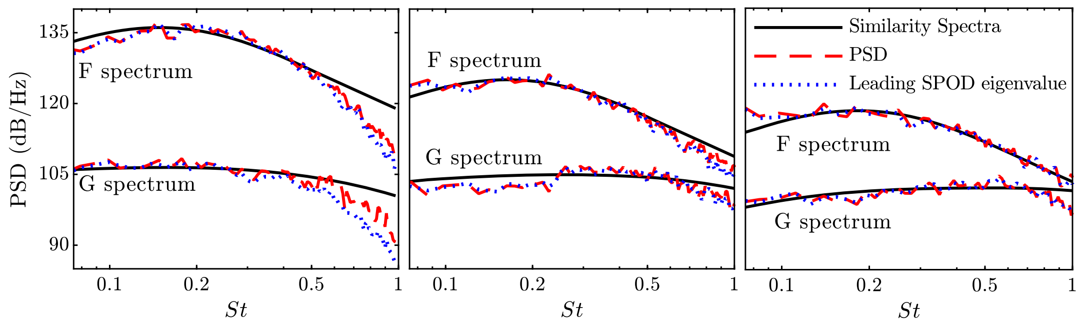

a) Supersonic jet $M_j = 1.5$ b) Transonic jet $M_j = 0.9$ c) Subsonic jet $M_j = 0.7$

Fig. 15 Comparison of F and G spectra with PSD (red dashed lines) and the leading SPOD eigenvalues (blue dotted lines). The contributions from the first three azimuthal wavenumbers $m = 0, 1, 2$ are summed.

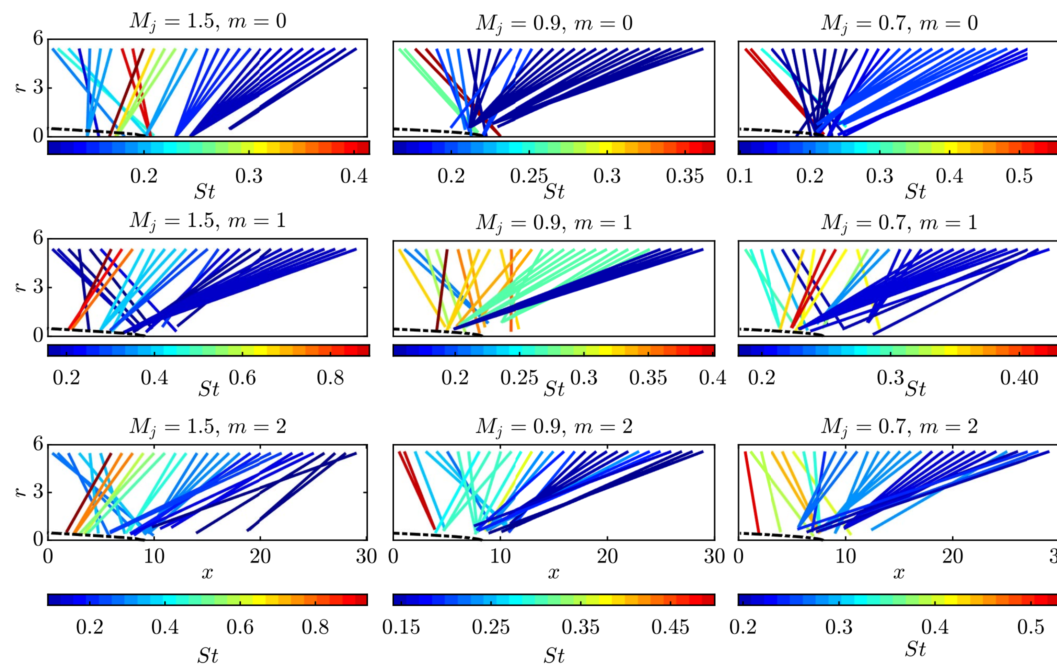

a) Supersonic jet $M_j = 1.5$ b) Transonic jet $M_j = 0.9$ c) Subsonic jet $M_j = 0.7$

Fig. 16 Directivity plot obtained from directional SPOD analysis: straight lines connect far-field focus region to location of maximum absolute value of SPOD mode at peak frequency. Peak frequencies are indicated by false colors.

$St \approx 0.2$, in agreement with the experimental observations made by Tam et al. [11], Viswanathan [13], and Tam et al. [14]. The spectrum corresponding to the leading SPOD mode is also shown in Fig. 15; it too resembles the F and G spectra. These results indicate that the noise in the downstream and sideline directions at $r = 6$ is accurately represented by the leading SPOD eigenpair. This finding implies that the patterns shown in Figs. 11–14 are the main contributors to both sideline and downstream jet noise.

Figure 16 aims at summarizing our results in a compact and interpretable way by relating the origin of the acoustic beams, radiation angle, and peak frequency. First, the peak Strouhal number of the leading SPOD mode is selected for each ϕ or far-field location. Each line then connects the far-field location to the point corresponding to the absolute maximum of the mode $\|\psi^{(1)}_{St_{\text{peak}}}\|_\infty$. This point approximately tracks the origin of the beam and serves as a proxy for the source location (but not necessarily the source mechanism, as discussed in the context of Fig. 4 above). False colors indicate the corresponding peak frequency. A few trends are observed. The primary source location of the dominant downstream radiation appears to be located in the region surrounding the end of the potential core. Sideline radiation to low angles emanates from the jet shear layer or the end of the potential core. In most cases, the sideline radiation appears to be slaved to the directive downstream radiation. In all cases the source location is in the vicinity of the jet axis ($r \approx 0$) or the lipline ($r \approx 0.5$), i.e., in the region where the KH wavepackets (inside the shear-layer) and Orr-type wavepackets (downstream of the potential core) dominate the dynamics of the jet. As observed earlier, the dominant superdirective radiation occurs at frequencies of $St \approx 0.2$, whereas higher frequencies are observed in the sideline direction.

IV. Conclusions

The first three azimuthal wavenumber components of supersonic, transonic, and subsonic jets are analyzed using SPOD with localized weighting. The dominant component is $m = 1$ for the supersonic jet and $m = 0$ for the subsonic case. In the transonic regime, $m = 1$ for $\phi \leq 150°$ is surpassed by $m = 0$ for $\phi > 150°$. In the sideline direction ($\phi 130°$), the $m = 1$ and $m = 2$ components are relatively more important. For all cases, the frequency of the peak PSD in the $m = 0$ component occurs for $St \approx 0.2$. The SPOD analysis identifies a single directive beam at $\phi \approx 160°$ as the corresponding radiation pattern. The source of this superdirective beam is at the end of the potential core for low frequencies and in the shear layer for higher frequencies. Suboptimal SPOD modes show multidirective patterns that include radiation in the upstream and sideline directions. For the first few modes, a clear hierarchy is observed that directly relates the mode number to the number of beams. Additional data may further confirm this finding by improving convergence of the SPOD. Noise in the sideline direction is in most cases associated with higher frequencies. The SPOD modes reveal that the largest contributions to noise emissions in the sideline and downstream directions both take the form of acoustic beams that originate from the end of the potential core. The inspection of modes at different angles and suboptimal modes further underlines the notion that sideline and downstream radiations share the same source location. A comparison of the SPOD spectra with the OASPL shows that the first SPOD eigenvalue accurately approximates the overall sound pressure over all angles. This implies that the corresponding mode structure is the single largest contributor to directional noise. Despite the limited radial extent of the domain, our observations strongly suggest that sideline and upstream radiation patterns are associated with the same large-scale coherent structures as the dominant downstream radiation. A possible source mechanism that was previously investigated in the context of wavepacket modeling by Cavalieri and Agarwal [60], and that in line with this notion, is coherence decay. In particular, this paper proposes a scenario in which the distortion of a coherent KH wavepacket gives rise to multidirective burst events. Future SPOD-based jet noise models may further benefit from the observation that both the dominant downstream and sideline radiation patterns are part of a single SPOD basis.

Appendix: Convergence of SPOD Modes

Following Lesshafft et al. [61] and Sano et al. [62], the convergence of the SPOD modes is assessed by splitting the data into two parts containing 50% of the full data each. The similarity of SPOD modes is quantified in terms of a normalized inner product,

$$\beta_{i;k} = \frac{\langle \psi_k, \psi_{i;k} \rangle_x}{\|\psi_k\|_x \cdot \|\psi_{i;k}\|_x} \tag{A1}$$

of the kth mode $\psi_{i;k}$ from subset i with the kth mode ψ_k from the full data. Here, $i = 1, 2$ indicates the two subsets. As before, the inner product defined by Eq. (2) is used. Values of $\beta_{i;k}$ close to unity imply convergence.

Figure A1 shows this measure for $St = 0.2$, 0.4, 0.6, and 0.8. The two different weighting functions considered in this work, i.e., the full far field [top row; see Eq. (12)] and the focus region of $\phi = 156°$ [bottom row; see Eq. (13)] are considered for the supersonic jet and azimuthal wavenumber $m = 1$. Form the proximity of the values of $\beta_{i;k}$ for the two subsets and its high values of $\beta_{i;k} \gtrsim 0.8$, it can be concluded that at least the first three far-field modes are well converged. For the restricted focus region with $\phi = 156°$, the first six modes are converged, following the same argument. Similar observations were found by [61,62].

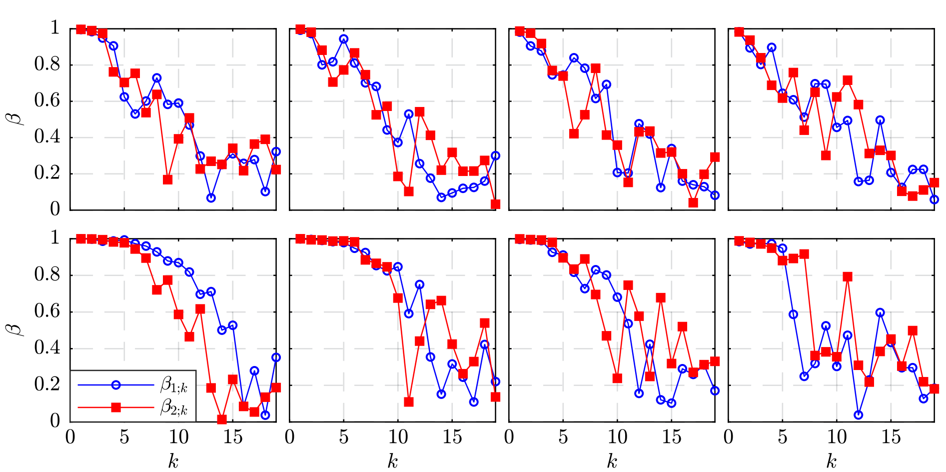

a) St **= 0.20** **b)** St **= 0.40** **c)** St **= 0.60** **d)** St **= 0.80**

Fig. A1 Convergence of SPOD modes for $M_j = 1.5$ and $m = 1$ at a) $St = 0.2$, b) $St = 0.4$, c) $St = 0.60$, and d) $St = 0.80$. The top and bottom rows show the convergence of the SPOD modes computed using the weighting function of the full far field [Eq. (12)] and the focus region of $\phi = 156°$ [Eq. (13)], respectively.

Acknowledgments

The authors thank Guillaume A. Brès for providing the jet large-eddy simulation (LES) data. The LES study was supported by the NAVAIR SBIR project, under the supervision of John T. Spyropoulos. The main LES calculations were carried out on CRAY XE6 machines at DoD HPC facilities in ERDC DSRC. The authors also thank the anonymous reviewers for their insightful comments and suggestions, which have improved the paper. A. Nekkanti thanks Sheel Nidhan for fruitful discussions and valuable comments.

References

[1] Crow, S. C., and Champagne, F., "Orderly Structure in Jet Turbulence," *Journal of Fluid Mechanics*, Vol. 48, No. 3, 1971, pp. 547–591. https://doi.org/10.1017/S0022112071001745

[2] Brown, G. L., and Roshko, A., "On Density Effects and Large Structure in Turbulent Mixing Layers," *Journal of Fluid Mechanics*, Vol. 64, No. 4, 1974, pp. 775–816. https://doi.org/10.1017/S002211207400190X

[3] Mollo-Christensen, E., "Jet Noise and Shear Flow Instability Seen from an Experimenter's Viewpoint," *Journal of Applied Mechanics*, Vol. 34, No. 1, 1967, pp. 1–7. https://doi.org/10.1115/1.3607624

[4] Michalke, A., "Instability of a Compressible Circular Free Jet with Consideration of the Influence of the Jet Boundary Layer Thickness," NASA TM 75190, 1977.

[5] Crighton, D., and Gaster, M., "Stability of Slowly Diverging Jet Flow," *Journal of Fluid Mechanics*, Vol. 77, No. 2, 1976, pp. 397–413. https://doi.org/10.1017/S0022112076002176

[6] Tam, C. K., and Morris, P. J., "The Radiation of Sound by the Instability Waves of a Compressible Plane Turbulent Shear Layer," *Journal of Fluid Mechanics*, Vol. 98, No. 2, 1980, pp. 349–381. https://doi.org/10.1017/S0022112080000195

[7] Tam, C. K., and Burton, D. E., "Sound Generated by Instability Waves of Supersonic Flows. Part 1. Two-Dimensional Mixing Layers," *Journal of Fluid Mechanics*, Vol. 138, Jan. 1984, pp. 249–271. https://doi.org/10.1017/S0022112084000112

[8] Crighton, D., and Huerre, P., "Shear-Layer Pressure Fluctuations and Superdirective Acoustic Sources," *Journal of Fluid Mechanics*, Vol. 220, Nov. 1990, pp. 355–368. https://doi.org/10.1017/S0022112090003299

[9] Jordan, P., and Colonius, T., "Wave Packets and Turbulent Jet Noise," *Annual Review of Fluid Mechanics*, Vol. 45, Jan. 2013, pp. 173–195. https://doi.org/10.1146/annurev-fluid-011212-140756

[10] Cavalieri, A. V., Jordan, P., Colonius, T., and Gervais, Y., "Axisymmetric Superdirectivity in Subsonic Jets," *Journal of Fluid Mechanics*,

Vol. 704, Aug. 2012, pp. 388–420.
https://doi.org/10.1017/jfm.2012.247

[11] Tam, C., Golebiowski, M., and Seiner, J., "On the Two Components of Turbulent Mixing Noise from Supersonic Jets," *Aeroacoustics Conference*, AIAA Paper 1996-1716, 1996.
https://doi.org/10.2514/6.1996-1716

[12] Viswanathan, K., "Analysis of the Two Similarity Components of Turbulent Mixing Noise," *AIAA Journal*, Vol. 40, No. 9, 2002, pp. 1735–1744.
https://doi.org/10.2514/2.1878

[13] Viswanathan, K., "Aeroacoustics of Hot Jets," *Journal of Fluid Mechanics*, Vol. 516, Oct. 2004, pp. 39–82.
https://doi.org/10.1017/S0022112004000151

[14] Tam, C. K., Viswanathan, K., Ahuja, K., and Panda, J., "The Sources of Jet Noise: Experimental Evidence," *Journal of Fluid Mechanics*, Vol. 615, Nov. 2008, pp. 253–292.
https://doi.org/10.1017/S0022112008003704

[15] Nichols, J. W., and Lele, S. K., "Global Modes and Transient Response of a Cold Supersonic Jet," *Journal of Fluid Mechanics*, Vol. 669, Feb. 2011, pp. 225–241.
https://doi.org/10.1017/S0022112010005380

[16] Schmidt, O., Towne, A., Colonius, T., Jordan, P., Jaunet, V., Cavalieri, A. V., and Bres, G. A., "Super- and Multi-Directive Acoustic Radiation by Linear Global Modes of a Turbulent Jet," *22nd AIAA/CEAS Aeroacoustics Conference*, AIAA Paper 2016-2808, 2016.

[17] Gudmundsson, K., and Colonius, T., "Instability Wave Models for the Near-Field Fluctuations of Turbulent Jets," *Journal of Fluid Mechanics*, Vol. 689, Dec. 2011, pp. 97–128.
https://doi.org/10.1017/jfm.2011.401

[18] Rodriguez, D., Sinha, A., Bres, G. A., and Colonius, T., "Acoustic Field Associated with Parabolized Stability Equation Models in Turbulent Jets," *19th AIAA/CEAS Aeroacoustics Conference*, AIAA Paper 2013-2279, 2013.
https://doi.org/10.2514/6.2013-2279

[19] Rodriguez, D., Sinha, A., Brès, G. A., and Colonius, T., "Inlet Conditions for Wave Packet Models in Turbulent Jets Based on Eigenmode Decomposition of Large Eddy Simulation Data," *Physics of Fluids*, Vol. 25, No. 10, 2013, Paper 105107.
https://doi.org/10.1063/1.4824479

[20] Sinha, A., Rodriguez, D., Brès, G. A., and Colonius, T., "Wavepacket Models for Supersonic Jet Noise," *Journal of Fluid Mechanics*, Vol. 742, March 2014, pp. 71–95.
https://doi.org/10.1017/jfm.2013.660

[21] Rigas, G., Schmidt, O. T., Colonius, T., and Bres, G. A., "One Way Navier-Stokes and Resolvent Analysis for Modeling Coherent Structures in a Supersonic Turbulent Jet," *23rd AIAA/CEAS Aeroacoustics Conference*, AIAA Paper 2017-4046, 2017.
https://doi.org/10.2514/6.2017-4046

[22] Schmidt, O. T., Towne, A., Colonius, T., Cavalieri, A. V., Jordan, P., and Brès, G. A., "Wavepackets and Trapped Acoustic Modes in a Turbulent Jet: Coherent Structure Eduction and Global Stability," *Journal of Fluid Mechanics*, Vol. 825, Aug. 2017, pp. 1153–1181.
https://doi.org/10.1017/jfm.2017.407

[23] Jeun, J., Nichols, J. W., and Jovanovic, M. R., "Input-Output Analysis of High-Speed Axisymmetric Isothermal Jet Noise," *Physics of Fluids*, Vol. 28, No. 4, 2016, Paper 047101.
https://doi.org/10.1063/1.4946886

[24] Jeun, J., and Nichols, J. W., "Wavepacket Modeling of Turbulent Jet Noise Generation Using Input-Output Analysis," *23rd AIAA/CEAS Aeroacoustics Conference*, AIAA Paper 2017-3378, 2017.
https://doi.org/10.2514/6.2017-3378

[25] Jeun, J., and Nichols, J. W., "Input-Output Analysis of Mach 0.9 Jet Noise," arXiv Preprint arXiv:1806.09280, 2018.

[26] Jeun, J., and Nichols, J. W., "Non-Compact Sources of Sound in High-Speed Turbulent Jets Using Input-Output Analysis," *2018 AIAA/CEAS Aeroacoustics Conference*, AIAA Paper 2018-3467, 2018.
https://doi.org/10.2514/6.2018-3467

[27] Towne, A., Schmidt, O. T., and Colonius, T., "Spectral Proper Orthogonal Decomposition and Its Relationship to Dynamic Mode Decomposition and Resolvent Analysis," *Journal of Fluid Mechanics*, Vol. 847, July 2018, pp. 821–867.
https://doi.org/10.1017/jfm.2018.283

[28] Schmidt, O. T., Towne, A., Rigas, G., Colonius, T., and Brès, G. A., "Spectral Analysis of Jet Turbulence," *Journal of Fluid Mechanics*, Vol. 855, Nov. 2018, pp. 953–982.
https://doi.org/10.1017/jfm.2018.675

[29] Schmidt, O. T., and Schmid, P. J., "A Conditional Space–Time POD Formalism for Intermittent and Rare Events: Example of Acoustic Bursts in Turbulent Jets," *Journal of Fluid Mechanics*, Vol. 867, May 2019, p. R2.
https://doi.org/10.1017/jfm.2019.200

[30] Papamoschou, D., "Wavepacket Modeling of the Jet Noise Source," *International Journal of Aeroacoustics*, Vol. 17, Nos. 1–2, 2018, pp. 52–69.
https://doi.org/10.1177/1475472X17743653

[31] Edgington-Mitchell, D., "Aeroacoustic Resonance and Self-Excitation in Screeching and Impinging Supersonic Jets—A Review," *International Journal of Aeroacoustics*, Vol. 18, Nos. 2–3, 2019, pp. 118–188.
https://doi.org/10.1177/1475472X19834521

[32] Taira, K., Brunton, S. L., Dawson, S. T., Rowley, C. W., Colonius, T., McKeon, B. J., Schmidt, O. T., Gordeyev, S., Theofilis, V., and Ukeiley, L. S., "Modal Analysis of Fluid Flows: An Overview," *AIAA Journal*, Vol. 55, No. 12, 2017, pp. 4013–4041.
https://doi.org/10.2514/1.J056060

[33] Rowley, C. W., and Dawson, S. T., "Model Reduction for Flow Analysis and Control," *Annual Review of Fluid Mechanics*, Vol. 49, Jan. 2017, pp. 387–417.
https://doi.org/10.1146/annurev-fluid-010816-060042

[34] Lumley, J. L., "The Structure of Inhomogeneous Turbulent Flows," *Atmospheric Turbulence and Radio Wave Propagation*, edited by A. M. Yaglom, and V. I. Tatarski, Nauka, Moscow, 1967, pp. 166–178.

[35] Lumley, J. L., *Stochastic Tools in Turbulence*, Courier Corp., Chelmsford, MA, 2007, Chap. 3.

[36] Sirovich, L., "Turbulence and the Dynamics of Coherent Structures. I. Coherent Structures," *Quarterly of Applied Mathematics*, Vol. 45, No. 3, 1987, pp. 561–571.
https://doi.org/10.1090/qam/910462

[37] Glauser, M. N., Leib, S. J., and George, W. K., "Coherent Structures in the Axisymmetric Turbulent Jet Mixing Layer," *Turbulent Shear Flows 5*, Springer, Berlin, 1987, pp. 134–145.
https://doi.org/10.1007/978-3-642-71435-1_13

[38] Citriniti, J., and George, W. K., "Reconstruction of the Global Velocity Field in the Axisymmetric Mixing Layer Utilizing the Proper Orthogonal Decomposition," *Journal of Fluid Mechanics*, Vol. 418, Sept. 2000, pp. 137–166.
https://doi.org/10.1017/S0022112000001087

[39] Jung, D., Gamard, S., and George, W. K., "Downstream Evolution of the Most Energetic Modes in a Turbulent Axisymmetric Jet at High Reynolds Number. Part 1. The Near-Field Region," *Journal of Fluid Mechanics*, Vol. 514, Sept. 2004, pp. 173–204.
https://doi.org/10.1017/S0022112004000163

[40] Welch, P., "The Use of Fast Fourier Transform for the Estimation of Power Spectra: A Method Based on Time Averaging over Short, Modified Periodograms," *IEEE Transactions on Audio and Electroacoustics*, Vol. 15, No. 2, 1967, pp. 70–73.
https://doi.org/10.1109/TAU.1967.1161901

[41] Brès, G. A., and Lele, S. K., "Modelling of Jet Noise: A Perspective from Large-Eddy Simulations," *Philosophical Transactions of the Royal Society of London, Series A: Mathematical and Physical Sciences*, Vol. 377, No. 2159, 2019, Paper 20190081.
https://doi.org/10.1098/rsta.2019.0081

[42] Brès, G. A., Jordan, P., Jaunet, V., Le Rallic, M., Cavalieri, A. V., Towne, A., Lele, S. K., Colonius, T., and Schmidt, O. T., "Importance of the Nozzle-Exit Boundary-Layer State in Subsonic Turbulent Jets," *Journal of Fluid Mechanics*, Vol. 851, Sept. 2018, pp. 83–124.
https://doi.org/10.1017/jfm.2018.476

[43] Brès, G. A., Ham, F. E., Nichols, J. W., and Lele, S. K., "Unstructured Large-Eddy Simulations of Supersonic Jets," *AIAA Journal*, Vol. 55, No. 4, 2017, pp. 1164–1184.
https://doi.org/10.2514/1.J055084

[44] Juve, D., Sunyach, M., and Comte-Bellot, G., "Filtered Azimuthal Correlations in the Acoustic Far Field of a Subsonic Jet," *AIAA Journal*, Vol. 17, No. 1, 1979, pp. 112–113.
https://doi.org/10.2514/3.61076

[45] Arndt, R. E., Long, D., and Glauser, M. N., "The Proper Orthogonal Decomposition of Pressure Fluctuations Surrounding a Turbulent Jet," *Journal of Fluid Mechanics*, Vol. 340, June 1997, pp. 1–33.
https://doi.org/10.1017/S0022112097005089

[46] Cavalieri, A. V., Jordan, P., Agarwal, A., and Gervais, Y., "Jittering Wave-Packet Models for Subsonic Jet Noise," *Journal of Sound and Vibration*, Vol. 330, Nos. 18–19, 2011, pp. 4474–4492.
https://doi.org/10.1016/j.jsv.2011.04.007.

[47] Zaman, K., "Flow Field and Near and Far Sound Field of a Subsonic Jet," *Journal of Sound and Vibration*, Vol. 106, No. 1, 1986, pp. 1–16.
https://doi.org/10.1016/S0022-460X(86)80170-5

[48] Bogey, C., Barré, S., Fleury, V., Bailly, C., and Juvé, D., "Experimental Study of the Spectral Properties of Near-Field and Far-Field Jet Noise,"

International Journal of Aeroacoustics, Vol. 6, No. 2, 2007, pp. 73–92. https://doi.org/10.1260/147547207781041868

[49] Lyrintzis, A., and Mankbadi, R., "Prediction of the Far-Field Jet Noise Using Kirchhoff's Formulation," *AIAA Journal*, Vol. 34, No. 2, 1996, pp. 413–416. https://doi.org/10.2514/3.13079

[50] Ffowcs Williams, J. E., and Hawkings, D. L., "Sound Generation by Turbulence and Surfaces in Arbitrary Motion," *Philosophical Transactions of the Royal Society of London, Series A: Mathematical and Physical Sciences*, Vol. 264, No. 1151, 1969, pp. 321–342. https://doi.org/10.1098/rsta.1969.0031

[51] Tinney, C., and Jordan, P., "The Near Pressure Field of Co-Axial Subsonic Jets," *Journal of Fluid Mechanics*, Vol. 611, Sept. 2008, pp. 175–204. https://doi.org/10.1017/S0022112008001833

[52] Tissot, G., Lajús, F. C., Jr., Cavalieri, A. V., and Jordan, P., "Wave Packets and Orr Mechanism in Turbulent Jets," *Physical Review Fluids*, Vol. 2, No. 9, 2017, Paper 093901. https://doi.org/10.1103/PhysRevFluids.2.093901

[53] Narayanan, S., Barber, T., and Polak, D., "High Subsonic Jet Experiments: Turbulence and Noise Generation Studies," *AIAA Journal*, Vol. 40, No. 3, 2002, pp. 430–437. https://doi.org/10.2514/2.1692

[54] Bishop, K., Williams, J. F., and Smith, W., "On the Noise Sources of the Unsuppressed High-Speed Jet," *Journal of Fluid Mechanics*, Vol. 50, No. 1, 1971, pp. 21–31. https://doi.org/10.1017/S002211207100243X

[55] Schlinker, R., Simonich, J., Shannon, D., Reba, R., Colonius, T., Gudmundsson, K., and Ladeinde, F., "Supersonic Jet Noise from Round and Chevron Nozzles: Experimental Studies," *15th AIAA/CEAS Aeroacoustics Conference (30th AIAA Aeroacoustics Conference)*, AIAA Paper 2009-3257, 2009. https://doi.org/10.2514/6.2009-3257

[56] Sasaki, K., Cavalieri, A. V., Jordan, P., Schmidt, O. T., Colonius, T., and Brès, G. A., "High-Frequency Wavepackets in Turbulent Jets," *Journal of Fluid Mechanics*, Vol. 830, Nov. 2017, p. R2. https://doi.org/10.1017/jfm.2017.659

[57] Zoppellari, E., Juve, D., Zoppellari, E., and Juve, D., "Reduction of Jet Noise by Water Injection," *3rd AIAA/CEAS Aeroacoustics Conference*, AIAA Paper 1997-1622, 1997. https://doi.org/10.2514/6.1997-1622

[58] Bogey, C., and Bailly, C., "An Analysis of the Correlations Between the Turbulent Flow and the Sound Pressure Fields of Subsonic Jets," *Journal of Fluid Mechanics*, Vol. 583, July 2007, pp. 71–97. https://doi.org/10.1017/S002211200700612X

[59] Freund, J. B., "Noise Sources in a Low-Reynolds-Number Turbulent Jet at Mach 0.9," *Journal of Fluid Mechanics*, Vol. 438, July 2001, pp. 277–305. https://doi.org/10.1017/S0022112001004414

[60] Cavalieri, A. V. G., and Agarwal, A., "Coherence Decay and Its Impact on Sound Radiation by Wavepackets," *Journal of Fluid Mechanics*, Vol. 748, June 2014, pp. 399–415. https://doi.org/10.1017/jfm.2014.186

[61] Lesshafft, L., Semeraro, O., Jaunet, V., Cavalieri, A. V., and Jordan, P., "Resolvent-Based Modeling of Coherent Wave Packets in a Turbulent Jet," *Physical Review Fluids*, Vol. 4, No. 6, 2019, Paper 063901. https://doi.org/10.1103/PhysRevFluids.4.063901

[62] Sano, A., Abreu, L. I., Cavalieri, A. V., and Wolf, W. R., "Trailing-Edge Noise from the Scattering of Spanwise-Coherent Structures," *Physical Review Fluids*, Vol. 4, No. 9, 2019, Paper 094602. https://doi.org/10.1103/PhysRevFluids.4.094602